

Cite this: *J. Mater. Chem. A*, 2023, **11**, 8277

# Solution phase treatments of $\text{Sb}_2\text{Se}_3$ heterojunction photocathodes for improved water splitting performance†

Pardis Adams,<sup>a</sup> Fabrizio Creazzo,<sup>a</sup> Thomas Moehl,<sup>a</sup> Rowena Crockett,<sup>b</sup> Peng Zeng,<sup>c</sup> Zbynek Novotny,<sup>de</sup> Sandra Lubner,<sup>a</sup> Wooseok Yang<sup>fg</sup> and S. David Tilley<sup>ib\*</sup>

Antimony selenide ( $\text{Sb}_2\text{Se}_3$ ) is an auspicious material for solar energy conversion that has seen rapid improvement over the past ten years, but the photovoltage deficit remains a challenge. Here, simple and low-temperature treatments of the p–n heterojunction interface of  $\text{Sb}_2\text{Se}_3/\text{TiO}_2$ -based photocathodes for photoelectrochemical water splitting were explored to address this challenge. The FTO/Ti/Au/ $\text{Sb}_2\text{Se}_3$  (substrate configuration) stack was treated with  $(\text{NH}_4)_2\text{S}$  as an etching solution, followed by  $\text{CuCl}_2$  treatment prior to deposition of the  $\text{TiO}_2$  by atomic layer deposition. The different treatments show different mechanisms of action compared to similar reported treatments of the back Au/ $\text{Sb}_2\text{Se}_3$  interface in superstrate configuration solar cells. These treatments collectively increased the onset potential from 0.14 V to 0.28 V vs. reversible hydrogen electrode (RHE) and the photocurrent from  $13 \text{ mA cm}^{-2}$  to  $18 \text{ mA cm}^{-2}$  at 0 V vs. RHE as compared to the untreated  $\text{Sb}_2\text{Se}_3$  films. From SEM and XPS studies, it is clear that the etching treatment induces a morphological change and removes the surface  $\text{Sb}_2\text{O}_3$  layer, which eliminates the Fermi-level pinning that the oxide layer generates.  $\text{CuCl}_2$  further enhances the performance due to the passivation of the surface defects, as supported by density functional theory molecular dynamics (DFT-MD) calculations, improving charge separation at the interface. The simple and low-cost semiconductor synthesis method combined with these facile, low-temperature treatments further increases the practical potential of  $\text{Sb}_2\text{Se}_3$  for large-scale water splitting.

Received 31st January 2023  
Accepted 20th March 2023

DOI: 10.1039/d3ta00554b

rsc.li/materials-a

## 1. Introduction

Meeting the increasing energy demand of today's world whilst attempting to achieve net zero emissions is one of the top priorities of this century. The sun's ample energy availability makes it a potential candidate to meet such demand in a green and sustainable manner.<sup>1</sup> Since solar-related energy sources are subject to weather fluctuations and the diurnal cycles, a practical solution is to store the energy in molecular bonds, as nature does through photosynthesis, such as those of  $\text{H}_2$ , which

can then be used as a fuel source. Therefore, the semiconductor-based conversion of solar energy to  $\text{H}_2$  by water splitting is advantageous for our already fuel-based economy to directly convert and store the energy within the same system.<sup>2–5</sup> The constraints on photoelectrochemical (PEC) water-splitting cells arise from three fundamental system requirements: efficient photogenerated charge collection, harvesting a substantial fraction of the available solar energy, and long-term stability. Due to the inherent area-dependency and hence the amount of material used, the predominant way to make PEC cells more competitive is by increasing their solar to hydrogen (STH) efficiency.<sup>6</sup>  $\text{Sb}_2\text{Se}_3$  has recently gained popularity due to its potential to have similar STH efficiencies to crystalline silicon, the benchmark material for solar conversion technology.  $\text{Sb}_2\text{Se}_3$  is a relatively cost-effective (Sb has a similar cost to Cu and Se has a similar cost to Sn) and reasonably abundant light-absorbing material, not listed as a “highly toxic” compound in many official records, as opposed to many other current semiconductor materials containing Cd and Pb.<sup>7</sup> The melting point of  $\text{Sb}_2\text{Se}_3$  lies at 608 °C, making it suitable for low-temperature processing and easy deposition. The  $\text{Sb}_2\text{Se}_3$  polycrystalline films have no other stable binary phase and a quasi-one-dimensional (Q1D) crystal structure oriented along the

<sup>a</sup>Department of Chemistry, University of Zurich, Zurich, Switzerland. E-mail: david.tilley@chem.uzh.ch

<sup>b</sup>Advanced Material and Surfaces, EMPA, Dübendorf, Switzerland

<sup>c</sup>Scientific Centre for Optical and Electron Microscopy (ScopeM), ETH, Zurich, Switzerland

<sup>d</sup>Swiss Light Source, Paul Scherrer Institute, Villigen-PSI, Switzerland

<sup>e</sup>Laboratory for Joining Technologies and Corrosion, EMPA, Dübendorf, Switzerland

<sup>f</sup>School of Chemical Engineering, Sungkyunkwan University (SKKU), Suwon, South Korea. E-mail: wooseok.yang@skku.edu

<sup>g</sup>SKKU Institute of Energy Science and Technology (SIEST), Sungkyunkwan University, Suwon 16419, Republic of Korea

† Electronic supplementary information (ESI) available. See DOI: <https://doi.org/10.1039/d3ta00554b>



[001] direction.<sup>8</sup> As opposed to other widely explored 3D photovoltaic absorbers such as CIGS and GaAs, the Q1D Sb<sub>2</sub>Se<sub>3</sub> has intrinsically benign grain boundaries (GB) along the ribbons and indeed at any crystallographic orientation due to the “self-healing” effect,<sup>9,10</sup> hence avoiding major surface recombination losses that limit high-efficiency thin-films. As a light absorber material for solar cells, Sb<sub>2</sub>Se<sub>3</sub> was first reported in 2014. Since then, the conversion efficiency has rapidly increased from 2.26% to 9.2% and recently to over 10.0% when alloyed with sulphur (Sb<sub>2</sub>(S, Se)<sub>3</sub>).<sup>11–13</sup> Even though within the PEC world, efficiencies are still low, with its optimal band gap at ~1.2 eV high absorption coefficient (>10<sup>5</sup> cm<sup>-1</sup> in the ultraviolet and visible spectrum) and resistance to photo corrosion, Sb<sub>2</sub>Se<sub>3</sub> is a prime candidate as a photoabsorber material for solar water splitting.<sup>14–16</sup> A key challenge currently limiting the device performance is the low open circuit voltage ( $V_{oc}$ ), mainly attributed to Sb<sub>Se</sub> antisite defects with mid-gap transition levels that can act as recombination centres.<sup>17–19</sup> There are several common approaches to tackle this complex problem, such as the passivation of surface states by optimisation of the device structure considering the lattice matching between layers,<sup>20</sup> an adaptation of the carrier extraction selectivity at the interface,<sup>17</sup> and modification of the band alignment.<sup>21</sup>

In this study, the focus was placed on increasing the onset potential of the Sb<sub>2</sub>Se<sub>3</sub> photocathode by interfacial engineering, more precisely through surface modification of the photoactive material.<sup>22</sup> It is well-known that at the semiconductor interface, the presence of surface states acts as trapping sites and recombination centres.<sup>23,24</sup> Therefore, simple, low-cost, and scalable solution-based treatments using earth-abundant chemicals with comparatively low toxicities were used in this study to passivate the above-mentioned surface states and, in turn, have better charge separation and reduced recombination. Several etchants have proven effective in removing the oxide layer on the Sb<sub>2</sub>Se<sub>3</sub> surface, of which (NH<sub>4</sub>)<sub>2</sub>S was chosen as the most promising due to its very low toxicity, good solubility in water and high etching rates without requiring additional heating.<sup>23</sup> As observed in other chalcogenides such as GaAs and Cu(In,Ga)Se<sub>2</sub>,<sup>23,24</sup> (NH<sub>4</sub>)<sub>2</sub>S is known to remove carbon impurities as well as the top oxide layer, which is often created as a result of dangling bonds' exposure to air at high temperatures during the selenisation process and thereafter until the overlayer is deposited. It could also incorporate sulphur onto the surface, which then passivates the dangling bonds on the surface.<sup>24,25</sup> CuCl<sub>2</sub> has been shown to have an effect on the performance of Sb<sub>2</sub>Se<sub>3</sub> solar cells in a superstrate configuration (*i.e.* by modifying the Sb<sub>2</sub>Se<sub>3</sub>/Au interface); however, the reason for this improvement is debated.<sup>26</sup> Therefore, we have undertaken a comprehensive study of different metal and halogen combinations as controls to elucidate the role of the CuCl<sub>2</sub> treatment and the (NH<sub>4</sub>)<sub>2</sub>S etching treatment. Density functional theory molecular dynamics (DFT-MD) was performed, finding a good agreement with the experimental observations, *i.e.*, Cu is binding to selenium atoms and passivating the surface states, therefore removing recombination centres and improving charge separation at the interface of the Sb<sub>2</sub>Se<sub>3</sub> and TiO<sub>2</sub>, which lead to the enhanced performance.

## 2. Results and discussion

The Sb<sub>2</sub>Se<sub>3</sub> compact films benefiting from high performances in this study were prepared by the selenisation of electrodeposited Sb films.<sup>14</sup> The film composition and structure in Fig. 1a are the basis of all films discussed in this study. Ti is used as a conductive anchoring layer to allow for better adhesion of the Au layer to the FTO substrate. The Au layer acts *via* an ohmic contact formation to the photo absorber as the hole-extracting contact. The photo absorber layer of Sb<sub>2</sub>Se<sub>3</sub> is then covered by a TiO<sub>2</sub> layer deposited by atomic layer deposition (ALD). The TiO<sub>2</sub> layer not only protects the active layer from eventual corrosion in the acidic media of the electrolyte but also forms a p–n junction with the photo absorber allowing for better charge separation. Finally, the Pt acts as a catalyst for the hydrogen evolution reaction (HER), facilitating enhanced charge transfer. With Fig. 1b, the experimental procedure of the etching and CuCl<sub>2</sub> treatment can be visualised. A large improvement in the performance of these films arises from the etching of the Sb<sub>2</sub>Se<sub>3</sub> surface with (NH<sub>4</sub>)<sub>2</sub>S solution, as well as treating the etched surface with a CuCl<sub>2</sub> solution. Each step of this procedure enhances both the photovoltage and photocurrent of the thin film. This increase can be observed in the cyclic voltammetry plots in Fig. 1c. Multiple CV experiments were undertaken to ensure reproducibility. With the statistical plot of multiple samples, the same increasing trend is observed, as seen in Fig. S1.† Whilst the untreated film gives ~13 mA cm<sup>-2</sup> at 0 V *vs.* reversible hydrogen electrode (RHE) with an onset potential of 0.14 V *vs.* RHE, the etched film shows an increased photovoltage of 0.22 V *vs.* RHE and a photocurrent of 15 mA cm<sup>-2</sup> at 0 V *vs.* RHE. The CuCl<sub>2</sub>-treated film is further improved with a photovoltage of 0.28 V *vs.* RHE and a photocurrent of 18 mA cm<sup>-2</sup> at 0 V *vs.* RHE. The incident photon to current efficiency (IPCE) spectrum of the Sb<sub>2</sub>Se<sub>3</sub> after etching and CuCl<sub>2</sub> treatment shows a stepwise increase in the quantum efficiency, increasing from 42% to 62% and further to 74% at 600 nm for the untreated, etched and etched + CuCl<sub>2</sub> treated films respectively (Fig. 1d). Integrations of the IPCE data were also obtained and plotted in Fig. S2a.† Fig S2b,† is an example of a typical (NH<sub>4</sub>)<sub>2</sub>S + CuCl<sub>2</sub> sample which clearly shows that the performance of the device is not directly proportional to the intensity of the light. Whilst IPCE is measured at ~1% sun (with the white light bias), the CV measurements are obtained at 100% sun and suffer from additional recombination losses at these higher light intensities. This light dependency can vary from sample to sample and is the reason for the discrepancy between the integrated current data and CV measurements in Fig. 1c. Stability measurements at 0.1 V *vs.* RHE in Fig. S2c† indicate a robust improvement of the treated samples and stability of over 4 hours. The decrease in stability likely results from the Pt catalyst detachment as after redeposition of Pt, most of the current is revived. Various control experiments were performed to understand the performance improvements' origin. These comparisons were undertaken with samples synthesised in the same batch so that any synthesis-to-synthesis variations could be eliminated. First, as seen in Fig. S3a,† the order of the treatments was reversed, such



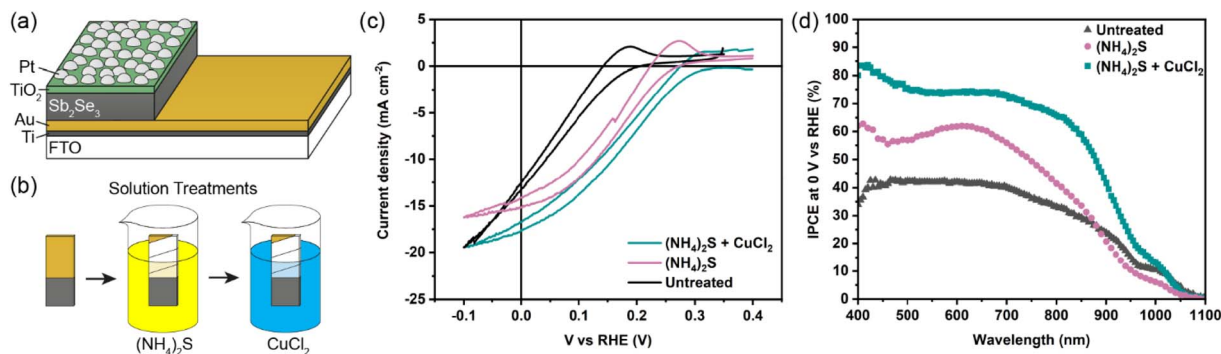


Fig. 1 (a) A schematic showing the device configuration of  $\text{Sb}_2\text{Se}_3$  photocathodes. All samples have an FTO/Ti/Au/ $\text{Sb}_2\text{Se}_3$ /TiO<sub>2</sub>/Pt configuration. The difference lies in the treatments undertaken before the TiO<sub>2</sub>/Pt layer deposition. (b) A schematic showing the  $(\text{NH}_4)_2\text{S}$  and  $\text{CuCl}_2$  treatment processes. Before the TiO<sub>2</sub>/Pt layers were deposited, the samples were wrapped in Teflon tape and etched/treated sequentially with  $(\text{NH}_4)_2\text{S}$  and  $\text{CuCl}_2$  solutions. (c) Current density vs. voltage plots of a typical sample in 1 M  $\text{H}_2\text{SO}_4$  under simulated 1 sun illumination. (d) Quantum efficiency spectra in 1 M  $\text{H}_2\text{SO}_4$  at 0 V vs. RHE under 1% sun-white light bias.

that films were first treated with  $\text{CuCl}_2$  and then etched with  $(\text{NH}_4)_2\text{S}$ , resulting in lower photovoltage and photocurrent than the champion  $\text{CuCl}_2$  treated sample of that batch (though still improved *versus* the untreated film). The performance of this reversed order sample is similar to the  $(\text{NH}_4)_2\text{S}$  treated sample without  $\text{CuCl}_2$  treatment, implying that the  $\text{CuCl}_2$  treatment is only effective after the etching process (blue curve in Fig. S3a†). It is hypothesised that this is due to Cu binding to the Se dangling bonds on the surface, which are absent before the etching process due to the surface  $\text{Sb}_2\text{O}_3$  layer (*vide infra*). In addition, an annealing treatment (at 200 °C for 20 minutes) after the  $\text{CuCl}_2$  treatment was investigated as it may facilitate the incorporation of  $\text{CuCl}_2$  into lattice sites of the  $\text{Sb}_2\text{Se}_3$  film. This experiment showed that further annealing does not increase the performance, meaning that the activation energy of the  $\text{CuCl}_2$  treatment is low and likely does not involve substitution at a lattice site (Fig. S3a,† red CV curve). Also, other chloride and copper sources were tested *via* other metal salts ( $\text{MgCl}_2$ ,  $\text{CsCl}$  and  $\text{Cu}(\text{NO}_3)_2$ ). The solutions were produced with the same concentration and in the same solvent to minimise the effects of external factors. Fig. S3b† shows that whilst the  $\text{MgCl}_2$  in ammonia solution precipitated to produce  $\text{Mg}(\text{OH})_2$  and hence had an entirely different and even detrimental effect on the sample, the  $\text{CsCl}$  showed almost no difference as compared to the untreated sample of that batch. On the other hand,  $\text{Cu}(\text{NO}_3)_2$  revealed an effect similar to  $\text{CuCl}_2$  and within

the range of error. The experiments showed that although Cu generally influences the performance of the photocathode, Cl does not affect the performance at all. Fig. 2a highlights morphological differences between the three samples *via* scanning electron microscopy (SEM). It shows that whilst the untreated sample has smooth and homogenous grain surfaces, the etched sample (Fig. 2b) is visibly roughened. The etched +  $\text{CuCl}_2$  treated sample (Fig. 2c), however, shows a similar morphological composition to the etched samples, which is in line with the fact that the Cu has negligible structural effects as it only targets the topmost Se atoms. This can also be observed in images obtained from atomic force microscopy-Kelvin probe force microscopy (KP-FM) in Fig. S4.† X-ray diffraction (XRD) measurements revealed a (*hkl*) preferential orientation among all samples. The XRD data also indicate that there are no significant differences (*i.e.*, changes in lattice spacing or preferential orientation) between the three different samples (Fig. S5†). To further understand the changes incurred by the different treatments, core levels of the main elements in the samples were measured by X-ray photoelectron spectroscopy (XPS). A significant change was observed in the Sb core level before and after the etching treatment (Fig. 3a and b). The higher binding energy shoulders observed around 530 eV and 540 eV denoted as  $\text{Sb}_2\text{O}_3$ , as well as the oxygen 1s peak at 532 eV, indicate surface oxidation due to atmospheric exposure of the dangling bonds of the bare  $\text{Sb}_2\text{Se}_3$  film after fabrication. This



Fig. 2 SEM images for an FTO/Ti/Au/ $\text{Sb}_2\text{Se}_3$  sample (a) untreated, (b) etched *via*  $(\text{NH}_4)_2\text{S}$ , and (c) etched *via*  $(\text{NH}_4)_2\text{S}$  +  $\text{CuCl}_2$  treatment.





Fig. 3 Synchrotron-based XPS core level spectra of Sb 3d for (a) untreated  $\text{Sb}_2\text{Se}_3$  and (b)  $\text{Sb}_2\text{Se}_3$  etched with  $(\text{NH}_4)_2\text{S}$ . (c) Band alignment changes due to the  $\text{Sb}_2\text{O}_3$  layer (represented by the blue Gaussian) and surface states (represented by red dashes), measured by KP-FM and XPS valence band maxima (VBM). Band bending is represented as a sloping line due to the low doping (the space charge region is larger than the film thickness).

phenomenon has been observed in other studies, but whilst the oxide layer is deemed beneficial in the PV cells with a superstrate configuration (where the  $\text{Sb}_2\text{O}_3$  acts as a buffer layer at the  $\text{Sb}_2\text{Se}_3/\text{Au}$  interface, making the contact more selective for holes); this layer has a detrimental effect on the substrate configurations.<sup>27,28</sup> The  $\text{Sb}_2\text{O}_3$  induces a Fermi-level pinning effect, causing an unfavourable surface band bending (Fig. 3c, drawn without curvature due to the near intrinsic level of doping in the semiconductor and consequently the very wide space charge region). This phenomenon makes electron transfer across the interface unfavourable and decreases the photo-generated charges' lifetime. The Fermi level position was measured by XPS valence band maxima and KP-FM measurements (Fig. S4 and S6†). After removing the oxide layer by etching, a decrease in the work function is observed, which remains unchanged (within the experimental error) following the  $\text{CuCl}_2$  treatment. The similar valence band maxima (VBM) measured by XPS indicates that the Cu does not dope the semiconductor and only acts to passivate the surface states. As seen in Fig. S7† diffuse reflectance spectroscopy (DRS) confirms that the band gap of the  $\text{Sb}_2\text{Se}_3$  remains the same after each treatment, which is in agreement with the band diagram in Fig. 3c and indicates that the treatments only target the surface of the samples.

Transmission electron microscopy (TEM) was used to closely observe the grains and grain boundaries for the three sample types. Fig. S8–S10† clearly show the distribution of elements, local structure, and crystallinity of different layers in these devices. However, no significant differences were observed between the three samples. EDX measurements following TEM were also undertaken in order to detect S or Cu near the surface or in the grain boundaries. Again, no significant differences were obtained from the EDX data. In Fig. S11† a line scan passing through two  $\text{Sb}_2\text{Se}_3$  grains and a grain boundary revealed a striking homogeneity of Sb, Se, Cu and Cl across grain boundaries, indicating that the amount of each element does not vary significantly throughout. This suggests that Cu does not tend to accumulate within the grain boundaries, contrary to the previous study showing the grain boundary inversion effect by the  $\text{CuCl}_2$  treatment on  $\text{Sb}_2\text{Se}_3$ .<sup>26</sup> To detect the low amount of S and Cu on the surface, time of flight mass spectrometry (ToF-SIMS) was employed. From Fig. 4a,

a substantial S signal is observed after the etching step and remains on the surface even after the  $\text{CuCl}_2$  treatment. The Cu content also increases after the  $\text{CuCl}_2$  treatment, as seen in Fig. 4b. Some Cu penetrates even further into the film; whilst this may be due to experimental noise, it may also be indicative of an exceedingly small amount of Cu making a bond with sublayer atoms. This behaviour is seen during DFT simulations and will be explained further in the next section. Both the S and the Cu content are highest at the surface. This coincides well with the lower amount of Sb and Se on the surface as opposed to the bulk (Fig. 4c). Similarly, from Fig. 4d, it can be observed that the  $\text{CuCl}_2$  treatment prevents the reoxidation of the photo absorber surface, allowing for a better interface with  $\text{TiO}_2$  as antimony oxide amounts on the surface also decrease and remain low after the etching treatment. Chloride content appears in all three films, which indicates that it may be present as a contaminant in the precursors from which the  $\text{Sb}_2\text{Se}_3$  is synthesised or from exposure to air prior to the measurement (Fig. S12†). Regardless, as chlorine has not been detected by any other methods and does not appear to have any effect when films are treated with other Cl sources, it can be concluded that Cl does not bind with or otherwise integrate into  $\text{Sb}_2\text{Se}_3$ . This is



Fig. 4 ToF-SIMS sputter depth profile for (a) sulphur, (b) copper, (c) antimony selenide, (d) antimony oxide.





in agreement with the literature in which chlorine is known to have a high formation enthalpy for interstitial doping, and the temperatures in this treatment are insufficient for the substitutional doping of this element into the  $\text{Sb}_2\text{Se}_3$  thin films.<sup>19</sup> Previous experimental studies also show that Cl ions tend to stay at the surface and not diffuse into the film. This is likely due to their large ion radius of 1.81 Å and electrostatic repulsive force, which can account for their negligible effects on device performance.

Spin-polarised DFT-MD was employed to shed light on the mechanism of action of the treatments. The (001)  $\text{Sb}_2\text{Se}_3$  surface was chosen as a suitable simplified representation of the surface of the polycrystalline films due to the preferential (*hkl*) orientation observed by XRD. The (001)  $\text{Sb}_2\text{Se}_3$  crystal was modelled where the ribbons had been cut, resulting in dangling bonds (Fig. 5a). 16 Cu ions were placed at the interface with the (001)  $\text{Sb}_2\text{Se}_3$ , and DFT-MD was performed at a temperature of 150 °C, which is the maximum temperature of the ALD chamber; the next synthesis step of these thin films. Analysing a 40 ps long DFT-MD trajectory, it was found that all the interfacial Cu ions moved towards the surface, making covalent bonds with the (001)  $\text{Sb}_2\text{Se}_3$  surface. In particular, all Cu ions are surface adsorbed, making (on average) 2 bonds with Se surface atoms at a distance of 2.3 Å as highlighted by the first peak position of the radial distribution function between surface Se atoms and Cu ions in Fig. 5b. Cu ions become coordinatively saturated once adsorbed at the surface, finding their 'equilibrium' position.

The temperature of 150 °C does not seem to be enough to break Cu–Se surface bonds and drive Cu ions into the  $\text{Sb}_2\text{Se}_3$  structure (channels). The average position of the bound Cu ions during the DFT-MD simulation has been found at the level of the (001)  $\text{Sb}_2\text{Se}_3$  surface, which involves a local distortion into the regular crystalline geometry of the (001)-surface pattern.

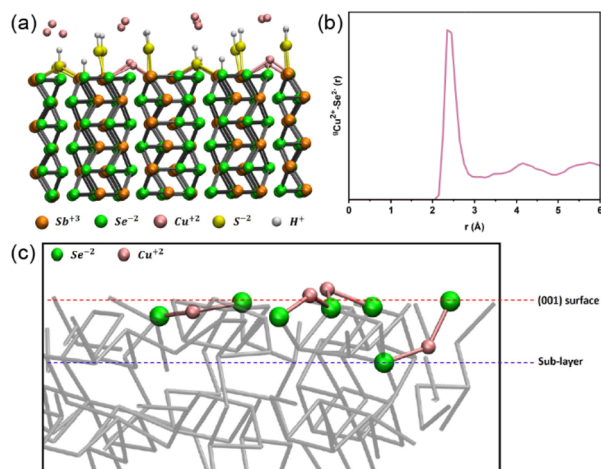


Fig. 5 (a) Zoom-in view of the simulation box: (001)  $\text{Sb}_2\text{Se}_3$  at the interface with 16 Cu atoms. Each Sb surface atom is terminated by S–H, and some Se surface atoms are terminated by hydrogen atoms (see text for details). Antimony atoms are presented in orange, and selenium atoms are in green. Sulphur atoms in yellow and hydrogen in white colour, respectively. (b) Radial distribution function between surface Se atoms and Cu ions. (c) Average position of Cu ions (in pink colour) during the simulation time.

However, during the DFT-MD, only one Cu atom (out of the 16 Cu atoms placed initially at the interface) positions itself between the (001) surface and the sublayer of the solid structure, evidencing a slightly more penetrating behaviour (binding to one surface Se atom and one sublayer Se atom) as shown in Fig. 5c. Although this could be ascribed to Cu-motion ('fluctuations') around the equilibrium position at the surface, it would be in line with the ToF-SIMS measurements where Cu atoms have been observed in the outermost layers of the slab. The calculation showed that Cu ions could bind to the Se ions at the (001) surface of  $\text{Sb}_2\text{Se}_3$ . Together with the experimental observations, in which the performance was enhanced by the  $\text{CuCl}_2$  treatment with favourable band bending, it implies that forming the Cu–Se bonds can passivate the detrimental surface states.

### 3. Experimental

#### 3.1 Synthesis of $\text{Sb}_2\text{Se}_3$ photocathode

The FTO TEC 15 substrates from Pilkington were cleaned by consecutive washing in water and ethanol in an ultrasonic bath and treated for 30 minutes under UV/ozone to remove surface contaminants. 10 nm of Ti adhesion layer and 150 nm of Au were coated onto the FTO substrates using a Safematic CCU-010 sputter coater. In a three-electrode configuration, Sb metal was electrodeposited on top of the FTO/Ti/Au substrates. The Sb solution (100 mL) consisting of 15 mM potassium antimony tartrate  $\text{K}_2\text{Sb}_2(\text{C}_4\text{H}_2\text{O}_6)_2$  (Sigma-Aldrich,  $\geq 99\%$ ) and 50 mM tartaric acid (Acros Organics, 99.5%) was adjusted to a pH of 1.3 (pH adjusted using conc. sulfuric acid, (Sigma-Aldrich,  $\geq 99\%$ )). To electrodeposit the Sb, a potential of  $-0.3$  V vs. Ag/AgCl was applied, and the thickness of the Sb metal was controlled by limiting the charge passed to  $1.4$  C  $\text{cm}^{-2}$ .<sup>14,29</sup> A two-zone furnace was used to selenise the electrodeposited Sb substrate. 30 mg of selenium pellets were placed symmetrically around the Sb substrate, and the chamber was purged with argon. A ramping rate of  $15$  °C  $\text{min}^{-1}$  was used to reach  $350$  °C, and the sample was held at this temperature for 40 min under static argon. After this 60 minute procedure, the furnace lid was opened to cool down the tube to room temperature, requiring approximately 60 minutes. After the selenisation, the exposed area of the Au layer (*i.e.*, where Sb was not deposited) remains the same colour and is still conductive, indicating that the Au layer is stable during this process. This simple synthesis method enables the fabrication of high-quality compact thin films without requiring sophisticated high vacuum equipment. However, small leaks in the gas connection to the tube may cause a  $\text{Sb}_2\text{O}_3$  layer to form on top of the  $\text{Sb}_2\text{Se}_3$ . Also, the selenisation process converts Sb metal to  $\text{Sb}_2\text{Se}_3$ , and therefore some unreacted Sb metal may remain in the final photoabsorber layer. This largely differs from other methods directly using a  $\text{Sb}_2\text{Se}_3$  precursor. When using this electrodeposition-based method, the designated deposition area must be closely monitored in order to have reproducible thickness and performance. A 100 nm thick layer of  $\text{TiO}_2$  was deposited *via* atomic layer deposition (ALD) using a Picosun R200 system. Ti and O were sourced from tetrakis(dimethylamido)titanium (TDMAT), and  $\text{H}_2\text{O}$ . The



temperature of the TDMAT precursor cylinder was held at 85 °C, and the reactor temperature at 120 °C. The thickness of the TiO<sub>2</sub> layer was confirmed by ellipsometry on a silicon witness wafer. In a final step, a nominally 2 nm thick layer of Pt was sputtered onto the photocathode.

### 3.2 Solution treatments

The exposed Au surface was protected with Teflon tape before all treatments. The Sb<sub>2</sub>Se<sub>3</sub> thin films were dipped for 5 s into a clear yellow aqueous (NH<sub>4</sub>)<sub>2</sub>S solution (Sigma-Aldrich, 40–48 wt% in H<sub>2</sub>O) (10 mL, 10–12 wt%) at room temperature, then rinsed for 10 s with distilled water and dried under N<sub>2</sub> flow. The CuCl<sub>2</sub> treatment was undertaken following the etching procedure. Films were dipped for 5 min into a clear dark blue aqueous CuCl<sub>2</sub> (Aldrich, 99%, powder) solution (10 mM in 28–30% in aqueous NH<sub>3</sub>) at room temperature. Subsequently, the samples were rinsed with distilled water for 10 s and dried under N<sub>2</sub> flow. The MgCl<sub>2</sub> (Sigma-Aldrich, anhydrous for synthesis), CsCl (Sigma-Aldrich, 99.9%) and Cu(NO<sub>3</sub>)<sub>2</sub> (Merck, Supelco, for analysis) solutions used for control experiments were prepared with the same concentration and solvent as the CuCl<sub>2</sub> solution (10 mM in 28–30% aqueous NH<sub>3</sub>). These treatments were likewise applied following the (NH<sub>4</sub>)<sub>2</sub>S etching step. As evident in Fig. S3a,† this quick dipping treatment at room temperature does not require further annealing or other energy-intensive equipment. The treatment solutions are also aqueous and non-toxic (as opposed to other etchants such as HF), making them simple to prepare and handle.

### 3.3 Photoelectrochemical (PEC) characterisation of Sb<sub>2</sub>Se<sub>3</sub>

The photoelectrochemical performance of the photocathodes was measured in a three-electrode configuration using a Bio-Logic SP-200 potentiostat under irradiation from simulated AM 1.5G illumination, calibrated using a silicon diode from PV Measurements, Inc. (100 mW cm<sup>2</sup>). A 1 M H<sub>2</sub>SO<sub>4</sub> (pH 0) solution was used for the measurements. The three-electrode configuration consisted of an Ag/AgCl (3 M KCl) reference electrode, a freshly cleaned Pt wire as the counter electrode and the photocathode as the working electrode. The CV was always measured with a scan speed of 10 mV s<sup>-1</sup> and scans were performed from positive to negative to positive potential. The photocathode area was defined by epoxying (Loctite 9461) around an O-ring (ID 7 mm) that was placed on the sample surface (Fig. S13†). IPCE was measured on a home built IPCE system featuring a halogen light source with a double monochromator and a white light bias from LED. The IPCE was measured in a three-electrode configuration as above at 0 V *vs.* RHE at 5 nm wavelength intervals and 1% white light bias.

### 3.4 Morphology and crystal characterisation

The plan view scanning electron microscopy (SEM) images of Sb<sub>2</sub>Se<sub>3</sub> thin films were measured using a Zeiss Gemini 450 SEM. X-ray diffraction (XRD) was obtained using the Rigaku Smartlab diffractometer. The Sb<sub>2</sub>Se<sub>3</sub> and Au reference cards were obtained from the Cambridge Crystallographic Data Centre (CCDC) database.

### 3.5 TEM and FIB sample preparation

TEM lamellae were prepared by FIB (Helios 5 UX, Thermo Fischer Scientific) using AutoTEM 5 (Thermo Fischer Scientific). Carbon deposition was used to protect the surface. The chunk milling and lamellae thinning were done at 30 kV with an FIB current from 20 nA to 90 pA. Then the lamellae were polished at 5 kV and finished at 2 kV. TEM characterisation was performed on a TEM (Talos F200X, Thermo Fischer Scientific) operating at 200 kV. EDS mapping was acquired by using quadrant EDS detectors (Super-X, Thermo Fischer Scientific, the Netherlands) in STEM mode.

### 3.6 XPS

Synchrotron XPS data (Fig. 3a and b) were acquired at the PHOENIX I (X07MB) beamline at the Swiss Light Source using an end station.<sup>30</sup> The spectra were acquired in a high vacuum (>1 × 10<sup>-5</sup> Pa) using a photon energy of 4000 eV and a pass energy of 100 eV. The energy scale was calibrated using an Au reference sample, setting the Au 4f<sub>7/2</sub> line to 84.0 eV. XPS depth profiling was conducted using a Physical Electronics (PHI) Quantum 2000 X-ray photoelectron spectrometer featuring monochromatic Al-Kα radiation generated from an electron beam operated at 15 kV and 32.3 W. The energy scale of the instrument was calibrated using an Au reference sample. The analysis was conducted at 1 × 10<sup>-6</sup> Pa, with an electron take-off angle of 45° and a pass energy of 23.50 eV. The neutraliser was set to automatic. In both cases, surface elemental concentrations were determined from the photoelectron spectra after Shirley background subtraction using the instrument-specific sensitivity factors for calculation. As necessary, the core level spectra were plotted to deconvolute spectra with contributions from multiple elements. An asymmetric line shape (GL 30) was assumed for the core level emissions with a separation of Δ*E* = 9.34 eV for the Sb 3d doublet.

### 3.7 KP-FM

An Asylum Research AFM (MFP-3D) was used to measure the work function of the samples. The probe used for the measurement was an AC240TM-R3. For calibration of the work function of the tip, a highly ordered pyrolytic graphite (HOPG) was used, with a reported work function of ~4.6 eV.<sup>31</sup> To achieve a fresh HOPG surface, a piece of scotch tape was used to pull off a few top layers of the graphite, exposing a fresh, clean surface for calibration. The HOPG used was purchased from Mikro-Masch (Grade: ZYA).

The open-source Gwyddion software package and the Asylum Research built-in software were used to analyse the AFM pictures further and determine the average work function of the surface.

### 3.8 ToF-SIMS

Secondary ion mass spectrometry measurements were conducted on a ToF-SIMS.5 from IONTOF GmbH, Germany. The instrument was operated in spectroscopy mode, and Bi<sup>+</sup> primary ions with an energy of 25 keV were used to analyse an area of 500 × 500 μm<sup>2</sup>. Sputtering was carried out with caesium



ions with an energy of 500 V. The sputtering time was correlated with sputter depth by measuring the sputtered area with a Dektak Stylus Profilometer (Bruker, Germany).

### 3.9 Computational

Spin-polarized DFT-MD simulation was performed in the Born-Oppenheimer framework employing the CP2K program package on (001)  $\text{Sb}_2\text{Se}_3$  at the interface with 16 Cu atoms.<sup>32,33</sup> 8 Cu atoms are initially placed at around 3 Å distance from the (001) surface, and 8 Cu atoms are initially placed at the height of the (001) surface. The (001)  $\text{Sb}_2\text{Se}_3$  slab consists of 240 atoms, where each Sb surface atom is terminated by S-H (some S-H are bridging two surface Sb atoms), and each Se atom is terminated by hydrogen atoms, as shown in Fig. 5a side view and in Fig. S14a† top view. The simulation box dimensions are  $x = 23.24$  Å,  $y = 23.54$  Å and  $z = 40.0$  Å. Periodic boundary conditions (PBCs) are applied in all 3-directions of space. A vacuum of around 15 Å has been inserted to separate the periodic z-replicas. The atoms were described by GTH pseudopotentials. The Perdew-Burke-Ernzerhof (PBE) exchange-correlation function was employed in agreement with previous works, which have shown a good description of the properties of  $\text{Sb}_2\text{Se}_3$ .<sup>19,34-36</sup> The DZVP-MOLOPT-SR basis set and a 400 Ry plane wave basis set for all atoms have been used, being a good compromise between computational cost and accuracy.<sup>37</sup> Grimme's D3 dispersion correction was employed.<sup>19,38,39</sup> The DFT-MD simulation was performed for ~40 ps in the NVT ensemble at a temperature of 150 °C (Nosé-Hoover chain thermostat) and adopted the Velocity-Verlet algorithm with a time step of 0.5 fs.<sup>40,41</sup> A uniform background charge and the Ewald summation for electrostatics take care of the total charge of the simulation box whenever necessary, as a standard procedure in DFT-MD simulations. The PBE functional was supplemented with the Hubbard  $U$  parameter in order to overcome the self-interaction error in the exchange and correlation of the over delocalized d- and f-orbitals (and the consequent underestimation of the  $\text{Sb}_2\text{Se}_3$  band gap).<sup>42-45</sup> Hubbard parameter  $U$  is known as the on-site Coulomb interaction energy.<sup>45</sup>  $U$  parameters have been calculated for  $\text{Sb}^{3+}$  and  $\text{Se}^{2-}$  atoms in order to reproduce the experimental band gap energy of around 1.2 eV of  $\text{Sb}_2\text{Se}_3$ . Values of  $U = 3$  eV,  $U = 2$  eV have been calculated and adopted for  $\text{Sb}^{3+}$  and  $\text{Se}^{2-}$  atoms, respectively. See ESI and Fig. S14 and S15† for modelling of the bulk crystalline structure of  $\text{Sb}_2\text{Se}_3$  and for bulk structural, electronic and mechanical properties calculations.

## 4. Conclusions

This study demonstrates enhanced photovoltage and photocurrent improvements through low-cost and room-temperature surface modification treatments. Overall, the etching treatment with  $(\text{NH}_4)_2\text{S} + \text{CuCl}_2$  on the surface of the  $\text{Sb}_2\text{Se}_3$  in substrate configuration improved the onset potential by 57% and the current density by 38%. This progressive improvement is due to the removal of the surface  $\text{Sb}_2\text{O}_3$  layer on the surface after the etching treatment. This is firmly evidenced by XPS. This layer

appears to cause an unfavourable surface band bending, causing surface recombination. Further improvement was also observed after  $\text{CuCl}_2$  solution treatment due to the binding of Cu to surface Se atoms which passivate the surface defects present on the surface of the material as a result of dangling bonds. The binding of Cu can be seen through ToF-SIMS and is supported by DFT calculations. As the stability, the light dependency and therefore the performance of the devices depends on the catalyst, further investigation can be done to address the loss of the catalyst itself and improve its durability. Despite the considerable improvement in the photovoltage *via* these simple surface treatments, there is still a significant loss of photovoltage due to bulk defects such as cation-anion anti-site defects.<sup>46</sup> Therefore, a better understanding and screening of other metal halides and nitrates, combined with our previously studied bulk passivation methods,<sup>47</sup> could pave the way towards improved performance in  $\text{Sb}_2\text{Se}_3$  photocathodes.

## Author contributions

S. D. T. and P. A. designed the experiment. W. Y. provided supervision and advice. P. A. fabricated and tested all the devices. F. C. undertook the DFT calculations. T. M. carried out the KP-FM and light intensity dependant measurements. R. C. and P. Z. performed the ToF-SIMS and FIB-TEM measurements, respectively. Z. N. operated and measured the XPS end station at the Swiss light source (SLS). S. L. provided supervision for the DFT calculations.

## Conflicts of interest

There are no conflicts to declare.

## Acknowledgements

This work was supported by the University of Zurich, URPP LightChEC, and SNF Project # 184737. P. A. thanks Jan Bühler for the figure designs and editing in this publication and Zhenbin Wang for the XRD measurement. We thank Selim Kazaz, Levin Häfliger, Thierry Eberhard, and Bernhard Fenner for preliminary studies. Z. N. acknowledges the PHOENIX I (X07MB) beamline of the Swiss Light Source, Paul Scherrer Institute, Villigen-PSI, Switzerland. This work was supported by a grant from the Swiss National Supercomputing Centre (CSCS) under project ID s1001. P. Z. acknowledge ScopeM for the support.

## Notes and references

- M. G. Walter, E. L. Warren, J. R. McKone, S. W. Boettcher, Q. Mi, E. A. Santori and N. S. Lewis, *Chem. Rev.*, 2010, **110**, 6446-6473.
- W. Yang, J. H. Kim, O. S. Hutter, L. J. Phillips, J. Tan, J. Park, H. Lee, J. D. Major, J. S. Lee and J. Moon, *Nat. Commun.*, 2020, **11**, 861.
- M. B. Costa, F. W. S. Lucas, M. Medina and L. H. Mascaro, *ACS Appl. Energy Mater.*, 2020, **3**, 9799-9808.





- 4 Y. Wang, R. Tang, L. Huang, C. Qian, W. Lian, C. Zhu and T. Chen, *ACS Appl. Mater. Interfaces*, 2022, **14**, 33181–33190.
- 5 K. Sivula and R. van de Krol, *Nat. Rev. Mater.*, 2016, **1**, 15010.
- 6 R. Sathre, C. D. Scown, W. R. Morrow, J. C. Stevens, I. D. Sharp, J. W. Ager, K. Walczak, F. A. Houle and J. B. Greenblatt, *Energy Environ. Sci.*, 2014, **7**, 3264–3278.
- 7 K. Zeng, D.-J. Xue and J. Tang, *Semicond. Sci. Technol.*, 2016, **31**, 063001.
- 8 Y. Ma, B. Tang, W. Lian, C. Wu, X. Wang, H. Ju, C. Zhu, F. Fan and T. Chen, *J. Mater. Chem. A*, 2020, **8**, 6510–6516.
- 9 Y. Zhou, L. Wang, S. Chen, S. Qin, X. Liu, J. Chen, D.-J. Xue, M. Luo, Y. Cao, Y. Cheng, E. H. Sargent and J. Tang, *Nat. Photonics*, 2015, **9**, 409–415.
- 10 R. E. Williams, Q. M. Ramasse, K. P. McKenna, L. J. Phillips, P. J. Yates, O. S. Hutter, K. Durose, J. D. Major and B. G. Mendis, *ACS Appl. Mater. Interfaces*, 2020, **12**, 21730–21738.
- 11 Y. Zhou, M. Leng, Z. Xia, J. Zhong, H. Song, X. Liu, B. Yang, J. Zhang, J. Chen, K. Zhou, J. Han, Y. Cheng and J. Tang, *Adv. Energy Mater.*, 2014, **4**, 1301846.
- 12 Z. Li, X. Liang, G. Li, H. Liu, H. Zhang, J. Guo, J. Chen, K. Shen, X. San, W. Yu, R. E. I. Schropp and Y. Mai, *Nat. Commun.*, 2019, **10**, 125.
- 13 X. Wang, R. Tang, C. Jiang, W. Lian, H. Ju, G. Jiang, Z. Li, C. Zhu and T. Chen, *Adv. Energy Mater.*, 2020, **10**, 2002341.
- 14 R. R. Prabhakar, W. Septina, S. Siol, T. Moehl, R. Wick-Joliet and S. D. Tilley, *J. Mater. Chem. A*, 2017, **5**, 23139–23145.
- 15 C. Chen, W. Li, Y. Zhou, C. Chen, M. Luo, X. Liu, K. Zeng, B. Yang, C. Zhang, J. Han and J. Tang, *Appl. Phys. Lett.*, 2015, **107**, 043905.
- 16 L. J. Phillips, C. N. Savory, O. S. Hutter, P. J. Yates, H. Shiel, S. Mariotti, L. Bowen, M. Birkett, K. Durose, D. O. Scanlon and J. D. Major, *IEEE J. Photovolt.*, 2019, **9**, 544–551.
- 17 A. Mavlonov, T. Razykov, F. Raziq, J. Gan, J. Chantana, Y. Kawano, T. Nishimura, H. Wei, A. Zakutayev, T. Minemoto, X. Zu, S. Li and L. Qiao, *Sol. Energy*, 2020, **201**, 227–246.
- 18 C. N. Savory and D. O. Scanlon, *J. Mater. Chem. A*, 2019, **7**, 10739–10744.
- 19 A. Stoliaroff, A. Lecomte, O. Rubel, S. Jovic, X. Zhang, C. Latouche and X. Roquefelte, *ACS Appl. Energy Mater.*, 2020, **3**, 2496–2509.
- 20 C. Chen and J. Tang, *ACS Energy Lett.*, 2020, **5**, 2294–2304.
- 21 W. Yang, R. R. Prabhakar, J. Tan, S. D. Tilley and J. Moon, *Chem. Soc. Rev.*, 2019, **48**, 4979–5015.
- 22 N. Guijarro, M. S. Prévot and K. Sivula, *Phys. Chem. Chem. Phys.*, 2015, **17**, 15655–15674.
- 23 M. Buffière, A.-A. El Mel, N. Lenaers, G. Brammertz, A. E. Zaghi, M. Meuris and J. Poortmans, *Adv. Energy Mater.*, 2015, **5**, 1401689.
- 24 J. Debehets, P. Himm, M. Menghini, S. A. Chambers, C. Marchiori, M. Heyns, J. P. Locquet and J. W. Seo, *Appl. Surf. Sci.*, 2018, **440**, 386–395.
- 25 H. Aibin, W. Wenwu and X. Qiuxia, *J. Semicond.*, 2009, **30**, 084001.
- 26 C. Chen, K. Li, S. Chen, L. Wang, S. Lu, Y. Liu, D. Li, H. Song and J. Tang, *ACS Energy Lett.*, 2018, **3**, 2335–2341.
- 27 C. H. Don, H. Shiel, T. D. C. Hobson, C. N. Savory, J. E. N. Swallow, M. J. Smiles, L. A. H. Jones, T. J. Featherstone, P. K. Thakur, T.-L. Lee, K. Durose, J. D. Major, V. R. Dhanak, D. O. Scanlon and T. D. Veal, *J. Mater. Chem. C*, 2020, **8**, 12615–12622.
- 28 H. Shiel, T. D. C. Hobson, O. S. Hutter, L. J. Phillips, M. J. Smiles, L. A. H. Jones, T. J. Featherstone, J. E. N. Swallow, P. K. Thakur, T.-L. Lee, J. D. Major, K. Durose and T. D. Veal, *J. Appl. Phys.*, 2021, **129**, 235301.
- 29 W. Septina, S. Ikeda, Y. Iga, T. Harada and M. Matsumura, *Thin Solid Films*, 2014, **550**, 700–704.
- 30 Z. Novotny, D. Aegerter, N. Comini, B. Tobler, L. Artiglia, U. Maier, T. Moehl, E. Fabbri, T. Huthwelker, T. J. Schmidt, M. Ammann, J. A. van Bokhoven, J. Raabe and J. Osterwalder, *Rev. Sci. Instrum.*, 2020, **91**, 023103.
- 31 M. M. Beerbom, B. Lägél, A. J. Cascio, B. V. Doran and R. Schlaf, *J. Electron Spectrosc. Relat. Phenom.*, 2006, **152**, 12–17.
- 32 J. Hutter, M. Iannuzzi, F. Schiffmann and J. Vandevondele, *Wiley Interdiscip. Rev.: Comput. Mol. Sci.*, 2014, **4**, 15–25.
- 33 J. Vandevondele, M. Krack, F. Mohamed, M. Parrinello, T. Chassaing and J. Hutter, *Comput. Phys. Commun.*, 2005, **167**, 103–128.
- 34 J. P. Perdew, K. Burke and M. Ernzerhof, *Phys. Rev. Lett.*, 1996, **77**, 3865–3868.
- 35 S. Goedecker, M. Teter and J. Hutter, *Phys. Rev. B: Condens. Matter Mater. Phys.*, 1996, **54**, 1703–1710.
- 36 R. Vadapoo, S. Krishnan, H. Yilmaz and C. Marin, *Phys. Status Solidi B*, 2011, **248**, 700–705.
- 37 J. Vandevondele and J. Hutter, *J. Chem. Phys.*, 2007, **127**, 114105.
- 38 J. Moellmann and S. Grimme, *J. Phys. Chem. C*, 2014, **118**, 7615–7621.
- 39 L. Goerigk, in *Non-Covalent Interactions in Quantum Chemistry and Physics*, Elsevier, 2017, pp. 195–219.
- 40 D. J. Evans and B. L. Holian, *J. Chem. Phys.*, 1985, **83**, 4069–4074.
- 41 L. Verlet, *Phys. Rev.*, 1967, **159**, 98–103.
- 42 C. Loschen, J. Carrasco, K. M. Neyman and F. Illas, *Phys. Rev. B*, 2007, **75**, 035115.
- 43 J. Hubbard, *Proc. R. Soc. London, Ser. A*, 1963, **276**, 238–257.
- 44 S. A. Tolba, K. M. Gameel, B. A. Ali, H. A. Almossalami and N. K. Allam, in *Density Functional Calculations - Recent Progresses of Theory and Application*, InTech, 2018.
- 45 V. I. Anisimov, J. Zaanen and O. K. Andersen, *Phys. Rev. B*, 1991, **44**, 943–954.
- 46 C. N. Savory and D. O. Scanlon, *J. Mater. Chem. A*, 2019, **7**, 10739–10744.
- 47 R. R. Prabhakar, T. Moehl, D. Friedrich, M. Kunst, S. Shukla, D. Adeleye, V. H. Damle, S. Siol, W. Cui, L. Gouda, J. Suh, Y. R. Tischler, R. van de Krol and S. D. Tilley, *Adv. Funct. Mater.*, 2022, **32**, 2112184.

